



The Faraday Rotation Measure of the M87 Jet at 3.5 mm with ALMA

Sijia Peng^{1,2,3} , Ru-Sen Lu^{1,4,5} , Ciriaco Goddi^{6,7,8,9} , Thomas P. Krichbaum⁵ , Zhiyuan Li^{2,3} , Ruo-Yu Liu^{2,3} ,
Jae-Young Kim^{10,5} , Masanori Nakamura^{11,12} , Feng Yuan¹³ , Liang Chen^{1,14} , Iván Martí-Vidal^{15,16} , and
Zhiqiang Shen^{1,4}

¹ Shanghai Astronomical Observatory, Chinese Academy of Sciences, Shanghai 200030, People's Republic of China; sjpeng@shao.ac.cn, rslu@shao.ac.cn

² School of Astronomy and Space Science, Nanjing University, Nanjing 210023, People's Republic of China

³ Key Laboratory of Modern Astronomy and Astrophysics, Nanjing University, Nanjing 210023, People's Republic of China

⁴ Key Laboratory of Radio Astronomy and Technology, Chinese Academy of Sciences, A20 Datun Road, Chaoyang District, Beijing, 100101, People's Republic of China

⁵ Max-Planck-Institut für Radioastronomie, Auf dem Hügel 69, D-53121 Bonn, Germany

⁶ Universidade de São Paulo, Instituto de Astronomia, Geofísica e Ciências Atmosféricas, Departamento de Astronomia, São Paulo, SP 05508-090, Brazil

⁷ Dipartimento di Fisica, Università degli Studi di Cagliari, SP Monserrato-Sestu km 0.7, I-09042 Monserrato, Italy

⁸ INAF—Osservatorio Astronomico di Cagliari, via della Scienza 5, I-09047 Selargius (CA), Italy

⁹ INFN, Sezione di Cagliari, Cittadella Univ., I-09042 Monserrato (CA), Italy

¹⁰ Department of Physics, Ulsan National Institute of Science and Technology, 50 UNIST-gil, Eonyang-eup, Ulju-gun, Ulsan 44919, Republic of Korea

¹¹ National Institute of Technology, Hachinohe College, 16-1 Uwanotai, Tamonoki, Hachinohe City, Aomori 039-1192, Japan

¹² Institute of Astronomy and Astrophysics, Academia Sinica, 11F of Astronomy-Mathematics Building, AS/NTU No. 1, Sec. 4, Roosevelt Road, Taipei 10617, Taiwan, R.O.C.

¹³ Center for Astronomy and Astrophysics and Department of Physics, Fudan University, Shanghai 200438, People's Republic of China

¹⁴ Key Laboratory for Research in Galaxies and Cosmology, Chinese Academy of Sciences, People's Republic of China

¹⁵ Departament d'Astronomia i Astrofísica, Universitat de València, C. Dr. Moliner 50, 46100 Burjassot, València, Spain

¹⁶ Observatori Astronòmic, Universitat de València, C. Catedrático José Beltrán 2, 46980 Paterna, València, Spain

Received 2024 February 21; revised 2024 September 9; accepted 2024 September 16; published 2024 October 29

Abstract

Faraday rotation is an important probe of the magnetic fields and magnetized plasma around active galactic nuclei jets. We present a Faraday rotation measure (RM) image of the M87 jet between 85.2 and 101.3 GHz with a resolution of $\sim 2''$ with the Atacama Large Millimeter/submillimeter Array. We found that the RM of the M87 core is $(4.5 \pm 0.4) \times 10^4 \text{ rad m}^{-2}$ with a low linear polarization fraction of $(0.88 \pm 0.08)\%$. The spatial RM gradient in the M87 jet spans a wide range from $\sim -2 \times 10^4 \text{ rad m}^{-2}$ to $\sim 3 \times 10^4 \text{ rad m}^{-2}$ with a typical uncertainty of $0.3 \times 10^4 \text{ rad m}^{-2}$. A comparison with previous RM measurements of the core suggests that the Faraday rotation of the core may originate very close to the supermassive black hole. Both an internal origin and an external screen with a rapidly varying emitting source could be possible. As for the jet, the RM gradient indicates a helical configuration of the magnetic field that persists up to the kiloparsec scale. Combined with the kiloparsec-scale RM measurements at lower frequencies, we found that RM is frequency-dependent in the jet. One possible scenario to explain this dependence is that the kiloparsec-scale jet has a trumpet-like shape, and the jet coil unwinds near its end.

Unified Astronomy Thesaurus concepts: [Low-luminosity active galactic nuclei \(2033\)](#); [Radio continuum emission \(1340\)](#); [Relativistic jets \(1390\)](#); [Extragalactic magnetic fields \(507\)](#); [Radio interferometry \(1346\)](#); [Polarimetry \(1278\)](#); [Radio galaxies \(1343\)](#)

1. Introduction

Magnetic fields are believed to play a vital role in the formation of relativistic jets (R. Blandford et al. 2019), either by extracting energy from a spinning supermassive black hole (SMBH) via the Blandford–Znajek mechanism (R. D. Blandford & R. L. Znajek 1977) or by tapping the rotational energy of a magnetized accretion flow, known as the Blandford–Payne mechanism (R. D. Blandford & D. G. Payne 1982). Detailed information of magnetic field strength and topology can be obtained by polarization observations (e.g., E. Clausen-Brown et al. 2011).

Faraday rotation of the polarization position angle occurs when the linearly polarized radiation travels through a magnetized plasma (B. J. Burn 1966). The amount of Faraday rotation is proportional to free electron density n_e (in cm^{-3})

along the propagation path and the magnetic field component (B_{\parallel} , unit in μG) along the line of sight (with the path length l in pc). The Faraday depth ($\phi(l)$) is defined as

$$\phi(l) = 0.81 \int_0^d n_e B_{\parallel} \cdot dl \text{ rad m}^{-2}. \quad (1)$$

Conventionally, a positive Faraday depth means that the magnetic field is pointing toward the observer. If there is only one source along the line of sight and it has no internal Faraday rotation, the observed Faraday depth would be equal to its Faraday rotation measure (RM). In this simplest case, the observed electron vector position angle (EVPA; χ_{obs}) of the target has a linear dependence on the square of the wavelength (λ^2):

$$\chi_{\text{obs}} = \chi_0 + \text{RM}\lambda^2, \quad (2)$$

where χ_0 is the intrinsic EVPA of the emission region. We can derive the RM by measuring the observed EVPA of the target at multiple wavelengths assuming that the opacity is the same at these wavelengths.



Original content from this work may be used under the terms of the [Creative Commons Attribution 4.0 licence](#). Any further distribution of this work must maintain attribution to the author(s) and the title of the work, journal citation and DOI.

The Faraday RM sign reversal spatially occurring across a jet has been found in a number of studies that suggest the existence of a helical magnetic field structure in a relativistic jet, such as the case of 3C273 (e.g., K. Asada et al. 2002). As a well-known target for studying SMBH physics, M87 ($D \approx 16.7 \pm 0.9$ Mpc, J. P. Blakeslee et al. 2009; S. Bird et al. 2010) launches a kiloparsec-scale FR-I type relativistic jet (F. N. Owen et al. 1980). Radio observations over the past two decades have intensively studied its jet from the arcsecond (e.g., F. N. Owen et al. 1990; H. L. Marshall et al. 2002; E. T. Meyer et al. 2013; C. Y. Kuo et al. 2014; S. S. Avachat et al. 2016; C. Goddi et al. 2021) to milliarcsecond scales (e.g., W. Junor et al. 1999; Y. Y. Kovalev et al. 2007; K. Asada & M. Nakamura 2012; K. Hada et al. 2016; J. Y. Kim et al. 2018; R. C. Walker et al. 2018; J. Park et al. 2019; Y. Cui et al. 2023; R.-S. Lu et al. 2023). However, robust evidence for the existence of an ordered large-scale helical magnetic field structure in its jet is still lacking. Using Hubble Space Telescope (HST) polarimetric imaging and Very Large Array (VLA) observations at 8–43 GHz, S. S. Avachat et al. (2016) found that an apparent helical structure in the EVPA exists in several jet knots on the kiloparsec scale. However, J. C. Algaba et al. (2016) pointed out that no significant RM gradient was found in the kiloparsec-scale jet based on their VLA observations, especially for a sign reversal of the transverse RM. Recently, A. Pasetto et al. (2021) reported a reversal of the RM sign across the M87 jet in knots E and F across the M87 jet from VLA observations at 4–18 GHz.

Polarization observations at millimeter wavelengths can also detect possible RM gradients. Due to less (differential) Faraday and opacity effects, a radio jet is usually more polarized at millimeter wavelengths (S. Trippe et al. 2010; S. Trippe 2014). Here, we present the first Faraday RM image of the M87 jet from 3.5 mm (Band 3) Atacama Large Millimeter/submillimeter Array (ALMA) observations. In Section 2, we describe our ALMA observations and data reduction. In Section 3, we show the polarization results and the RM variations along the jet. The analysis of the RM of the unresolved core and the kiloparsec-scale jet is discussed in Section 4. We summarize our results in Section 5.

2. Observation and Data Reduction

Our Cycle 5 ALMA observations of M87 (Project Code: 2017.1.00842.V) were performed on 2018 April 14–15, with 32 antennas of 12 m diameter at Band 3 using the C43-3 configuration. The maximum baseline length is 500 m, and the minimum length is 15 m. These observations cover 85.3–101.3 GHz with four full-polarization subbands (spectral windows, SPWs) centered at 86.3, 88.3, 98.3, and 100.3 GHz with a bandwidth of 1.875 GHz each (corresponding to a maximum detectable RM of 1.73×10^6 rad m⁻² and a minimum of $(4.8\text{--}19) \times 10^3$ rad m⁻²). The ALMA observations were performed in phased-array mode (L. D. Matthews et al. 2018; G. B. Crew et al. 2023) as part of the Global 3 mm VLBI Array (GMVA) imaging experiment (R.-S. Lu et al. 2023), and 3C 273 and 3C 279 were observed in interleaved scans as calibrators. The observation lasted about 8.0 hr, and the total on-source time for M87 was about 1.5 hr.

The ALMA interferometric data were calibrated with Common Astronomy Software Applications¹⁷ (CASA; version: 5.4.0) following the calibration procedures described in

C. Goddi et al. (2019). Since ALMA has linearly polarized feeds, a contribution from Stokes Q , U , and parallactic angle appears in the real part of all correlations (XX , YY , XY , YX). Here is a brief description of the polarization calibration procedures (C. Goddi et al. 2019). We first obtained gain solutions for the polarization calibrator (3C279). Next, the X - Y cross-phase offset of the reference antenna and the Stokes Q , U parameters for the polarization calibrator were determined simultaneously with the task `gaincal` in `XYf+QU` mode (3C279 has $\sim 130^\circ$ parallactic angle coverage). Finally, we solved for the instrumental polarization determining the leakage terms (or D-terms) for all antennas with the task `polcal`. The polarization leakage is of the order of a few percent and consistent across frequency bands.

As for imaging, the CASA `TCLEAN` task was applied to all Stokes parameters (I , Q , U , and V) data for each subband to obtain polarization images of M87. In the `TCLEAN` task, we set `NTERMS=2`, `CELL=0.2 arcsec`, and a Briggs weighting with `Robust=1`. We applied a primary beam correction and a manual mask that covers the regions from the core to the extended inner lobes of M87 in the `TCLEAN` procedure. The subband images in Stokes I have rms noise levels of 2.5, 2.2, 2.0, and 2.0 mJy beam⁻¹ and synthesized beams of $2''.9 \times 2''.3$, $2''.8 \times 2''.2$, $2''.5 \times 2''.1$, and $2''.4 \times 2''.0$ at 86.3, 88.3, 98.3, and 101.3 GHz, respectively. To obtain the image of linear polarized intensity, the CASA task `IMMATH` was used with the `POLI` mode. The linear polarized rms noise levels in each subband are 2.0, 2.0, 1.5, and 1.5 mJy beam⁻¹ at 86.3, 88.3, 98.3, and 101.3 GHz, respectively.

We used the `IMFIT` task to measure the polarized properties of the M87 core and the jet knots assuming elliptical Gaussian components. Table 1 displays these measurements at 86.3 GHz (SPW 0). Defined by $\chi = \frac{1}{2} \arctan(U/Q)$, the observed EVPA (χ_{obs}) was calculated with the `IMMATH` task in the `POLA` mode. The uncertainty of EVPA was calculated with the propagation of the standard error following the definition of χ . Following C. Goddi et al. (2021), the calculation also incorporates a 5% systematic error caused by the absolute flux-scale calibration and an additional 0.03% systematic error due to leakage from Stokes I to Stokes Q and U (corresponding to a minimum detectable polarization of 0.1%; A. Remijan et al. 2019); systematic errors were included in the calculation in a quadratic form.

To obtain the Faraday RM, clean images of the individual SPW were used. First, we tapered the visibilities of SPWs 1–3 and restored the image to match the lower resolution of SPW 0, which is $2''.9 \times 2''.3$ at P. A. = $-4^\circ.5$, by setting the `RESTORATION` parameters in the `TCLEAN` task. Each SPW was then separately imaged with the above `TCLEAN` parameters in full Stokes parameters. Finally, we applied the `RMFIT` task to the individual SPW images to make a Faraday RM image and the associated error map with a polarized threshold of 6 mJy beam⁻¹ ($3 \times$ rms). No systematic errors were included in `RMFIT`. We note that, in principle, ALMA can only guarantee polarization information within the inner 1/3 of the primary beam,¹⁸ i.e., approximately the inner $20''$ at Band 3. However, by checking the calibrators, we confirm that both on-axis ($\leq 20''$) and off-axis ($20''\text{--}60''$) polarization leakages are below the threshold of our polarization analysis (6 mJy beam⁻¹), which means the polarization leakage does

¹⁷ <https://casa.nrao.edu>

¹⁸ <https://almascience.eso.org/documents-and-tools/cycle5/alma-technical-handbook>

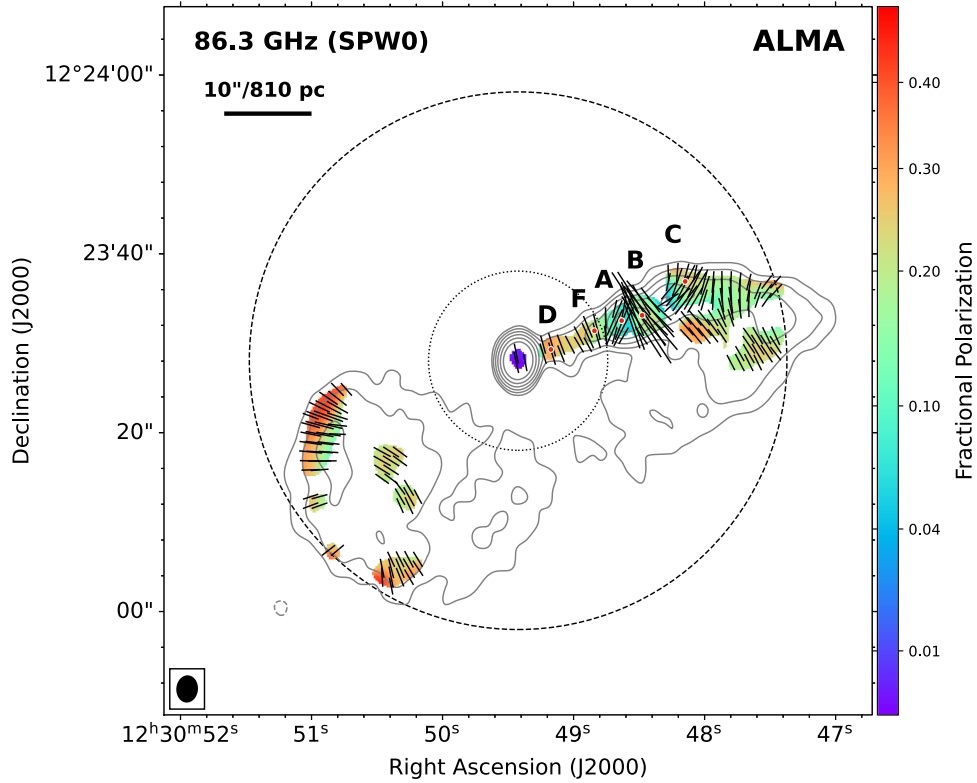


Figure 1. ALMA image of the continuum (contour) and linear polarization (color) image of the M87 central region at 86 GHz (SPW0), enclosing the core, the one-sided jet, and the two inner lobes. The dashed line denotes the FWHM of the primary beam, and the dotted line represents its inner 1/3 region of primary beam. The image center is at the M87 unresolved core. The gray contours starts at 4 times the Stokes I rms noise ($1.4 \text{ mJy beam}^{-1}$) and increase in steps of two. The linear polarized electron vectors are marked by the black sticks and only shown for regions where the polarized intensity is greater than 3 times the polarized rms level. The stick length is proportional to the polarized intensity. The synthesis beam, $2''.9 \times 2''.3, -4''.5$, is displayed as a filled ellipse at the bottom-left corner. The prominent knots A, B, C, and D are marked as red dots with white edges. We note that this image does not include systematic errors.

Table 1
Polarization Properties of M87 Core and the Selected Jet Knots at 86.3 GHz (SPW0) in 2018 April

Position (1)	Coordinate		$I_{\text{Stokes } I, \text{peak}}$ (mJy beam^{-1}) (4)	$I_{\text{pol, peak}}$ (mJy beam^{-1}) (5)	$I_{\text{pol, tot}}$ (mJy) (6)	EVPA ($^{\circ}$) (7)
	R.A. (2)	Decl. (3)				
Core	$12^{\text{h}}30^{\text{m}}49^{\text{s}}.423$	$+12^{\text{d}}23^{\text{m}}28^{\text{s}}.05$	1422 ± 10	8.3 ± 0.7	11.3 ± 1.3	11.7 ± 3.1
Knot A	$12^{\text{h}}30^{\text{m}}48^{\text{s}}.630$	$+12^{\text{d}}23^{\text{m}}32^{\text{s}}.50$	233 ± 18	18.4 ± 1.2	29.4 ± 2.9	-27.8 ± 4.8
Knot B	$12^{\text{h}}30^{\text{m}}48^{\text{s}}.474$	$+12^{\text{d}}23^{\text{m}}33^{\text{s}}.04$	209 ± 19	40.6 ± 2.0	55.1 ± 3.4	33.0 ± 3.2
Knot C	$12^{\text{h}}30^{\text{m}}48^{\text{s}}.146$	$+12^{\text{d}}23^{\text{m}}35^{\text{s}}.84$	87 ± 8	17.7 ± 1.3	39.4 ± 3.9	-34.0 ± 3.7
Knot D	$12^{\text{h}}30^{\text{m}}49^{\text{s}}.173$	$+12^{\text{d}}23^{\text{m}}29^{\text{s}}.30$	33 ± 3	9.6 ± 0.4	17.4 ± 0.8	16.8 ± 2.7
Knot F	$12^{\text{h}}30^{\text{m}}48^{\text{s}}.837$	$+12^{\text{d}}23^{\text{m}}31^{\text{s}}.34$	53 ± 5	11.1 ± 0.4	24.3 ± 1.1	17.6 ± 4.1

Note. (1) Selected positions measured by IMFIT. (2)–(3) J2000 coordinates of the fitted knot centroid. (4) The Stokes I peak flux density. (5) The peak polarized flux density. (6) The integrated polarized flux density. (7) The average EVPA in four SPWs at the centroid. The EVPA errors include a 5% systematic error in absolute flux-scale calibration and an additional 0.03% systematic error due to the leakage from Stokes I to Stokes Q , which are both included.

not significantly influence the polarization results and Faraday RM images. The latter showcase ordered polarization structures along and across the entire jet (see Figures 1 and 2), providing further indication that ALMA is capable of reliably recovering the polarized signal outside of the inner 1/3 beam (see also C. L. H. Hull et al. 2020).

3. Results

Figure 1 shows the 86.3 GHz linearly polarized intensity image for the central $1'$ region of M87, where the compact core, the northwest jet, and the two inner lobes are evident. The total

intensity (Stokes I) shown as gray contours illustrates the overall emission structure. The radio core dominates the Stokes I (total) flux with a peak brightness of $1.407 \pm 0.006 \text{ Jy beam}^{-1}$ derived from CASA IMFIT task. The jet knots, including knots A, B, C, D, and F, are more prominent in the linearly polarized intensity image than in the total intensity image. Specifically, the peak polarized flux density is found at knot B, with a peak flux density of $36.7 \pm 1.8 \text{ mJy beam}^{-1}$. In contrast, previous optical and radio (centimeter) observations pinpointed knot A as the peak in polarized intensity (E. S. Perlman et al. 1999; S. S. Avachat et al. 2016).

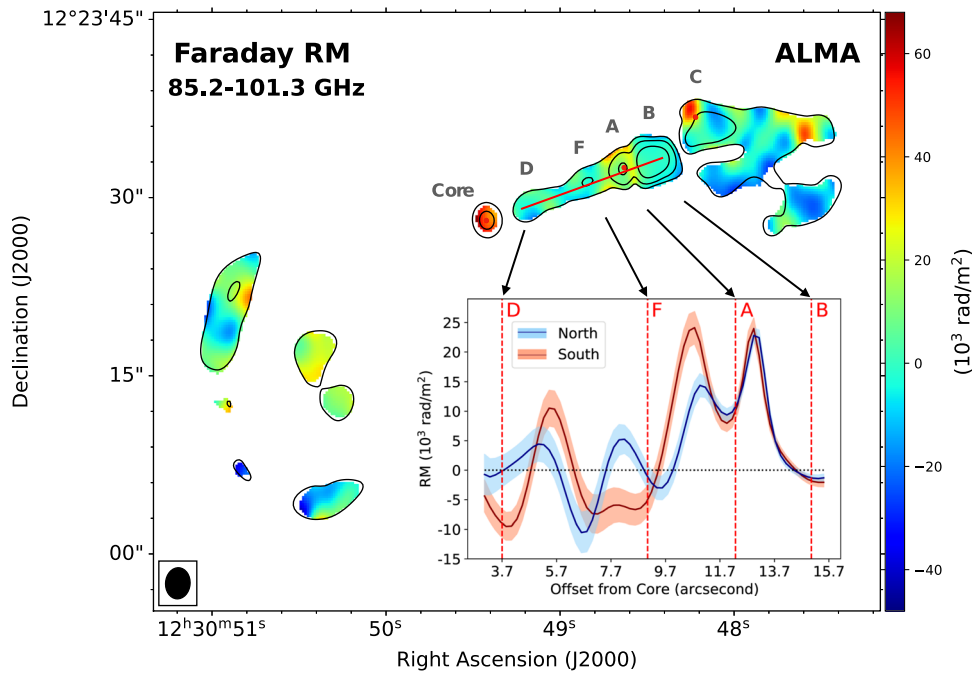


Figure 2. ALMA Faraday RM of the core, jet, and eastern inner lobe, overlaid with polarized intensity contours at levels of $(4, 8, 16, 32) \times 1.4 \text{ mJy beam}^{-1}$, the rms level of the polarized intensity. The positions of knots D, F, A, B, and C are marked as red dots with capital letters. The red dots mark the locations of the selected points, and their EVPA distributions at different frequencies are shown in Figure 4. The size of synthesis beam, $2''.9 \times 2''.3, -4''.5$, is displayed as a filled ellipse at the bottom-left corner. We note that this image does not include systematic errors. The insert shows RM variations on the northern (blue) and southern (red) side along the jet axis (red solid line), averaged over a width of $1''$. The dark red (blue) curve is encompassed by the orange (light blue) strip representing 1σ error. The red vertical dash lines mark the centroids of knots D, F, A, B, and C. The horizontal black dotted line marks the zero level of the RM.

The fractional polarization image, defined as the ratio of the linearly polarized intensity to the Stokes I intensity, is shown as the background color in Figure 1. The lowest fractional polarization is found in the core at a level of only $(0.88 \pm 0.08)\%$. The fraction increases to $(28.4 \pm 4.8)\%$ at knot D and gradually decreases downstream of the jet to only $(6 \pm 0.6)\%$ at knot A and rebounds to $(22.2 \pm 1.0)\%$ at knot B. The two inner lobes show an overall higher fractional polarization than the jet. In particular, values up to $(40\text{--}50)\%$ are seen along the edge of the eastern inner lobe, spatially corresponding to the shock due to the termination of the counter jet (W. B. Sparks et al. 1992; M. Stiavelli et al. 1992).

The black sticks in Figure 1 represent the EVPA, the length of which corresponds to the polarization intensity. The EVPA is highly aligned in the core and along the inner part of the jet out to knot F. The aligned EVPA between knot D and F indicates that the projected magnetic field, which is perpendicular to the EVPA, is well ordered and aligned with the jet. The EVPA becomes significantly distorted further downstream in the jet, especially in knots A and B, where the polarized intensities are the highest among the jet knots. The EVPA distribution along the jet (and the corresponding magnetic field topology) is strikingly similar to that obtained with ALMA at 1.3 mm (213–230 GHz) by C. Goddi et al. (2021; e.g., their Figure 2), including the substantial change of EVPA in knots A and B. The latter was also found in previous optical and radio polarimetric observations, suggesting the existence of a shock in the immediate upstream of knot A (S. S. Avachat et al. 2016). The eastern inner lobe exhibits an overall ordered EVPA, i.e., EVPA is constant or changes smoothly and continuously over several beams. In particular, the inferred projected magnetic field appears to be well aligned with the edge of the eastern inner lobe. The western lobe shows less

ordered EVPA, and there is no significant enhancement of fractional polarization along its edge. This difference could be due to the different ambient medium and pressure between the eastern and western inner lobes. It is suggested that a molecular gas with a total mass of $M_{\text{H}_2} \sim 4.7 \times 10^5 M_{\odot}$ exists outside the eastern lobe (A. Simionescu et al. 2018). The interstellar pressure is also different, as suggested by several X-ray cavities surrounding the eastern lobe and a huge shock cocoon on the north side of the western lobe (R. P. Kraft et al. 2005; E. T. Million et al. 2010). The linearly polarized intensity images of the other three subbands have the same structures as Figure 1 (SPW 0).

The spatial distribution of RM, as derived from the EVPA between 86.3 and 100.3 GHz following Equation (2), is shown in Figure 2, and Figure 3 displays the RM uncertainties.¹⁹ The EVPA vector at the radio core is spatially well ordered with a position angular range of $(0\text{--}15)^{\circ}$ at a resolution of $2''$. The RM distribution of the core varies in the range of $(3.5\text{--}6.6) \times 10^4 \text{ rad m}^{-2}$ and appears asymmetric, showing on-average higher (lower) values at the southeastern (northwestern) side, which is probably due to Laing–Garrington effect where the jet closer to us appears brighter and more polarized than its counter jet (S. T. Garrington et al. 1988; R. A. Laing 1988). The RM value at the core centroid ([R. A., decl.] = $[12^{\text{h}}30^{\text{m}}49^{\text{s}}.423, +12^{\circ}23'28''.05]$) is $(4.5 \pm 0.4) \times 10^4 \text{ rad m}^{-2}$. The average RM within a $1''$ -radius circle, approximately equal to the synthesized beam size, is $(4.9 \pm 0.9) \times 10^4 \text{ rad m}^{-2}$. This asymmetric RM distribution with a low northwest side and a high southeast side is not an artificial pattern because the distribution of RM errors in the

¹⁹ It is worth noting that both Figures 2 and 3 do not present any systematic errors, only the direct outputs from CASA task RMFIT.

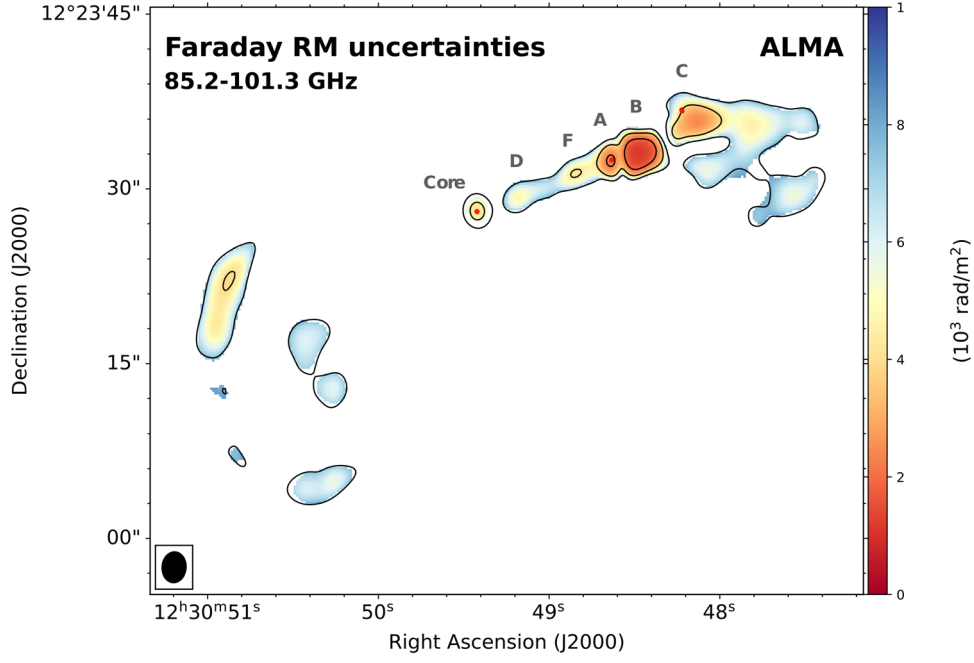


Figure 3. The uncertainties (one standard deviation) of Faraday RM of the core, jet, and eastern inner lobe, overlaid with polarized intensity contours at levels of (4, 8, 16, 32) $\times 1.4$ mJy beam $^{-1}$, the rms level of the polarized intensity. The positions of knots D, F, A, B, and C are marked with capital letters. The red dots mark the locations of the selected points, and their EVPA distributions at different frequencies are shown in Figure 4. The size of synthesis beam, $2''.9 \times 2''.3$, $-4''.5$, is displayed as a filled ellipse at the bottom-left corner. We note that this image does not include systematic errors.

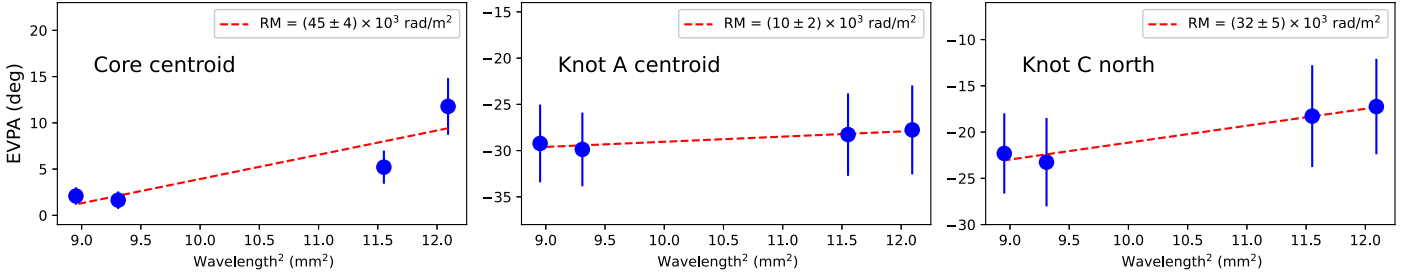


Figure 4. The EVPAs vs. λ^2 of the core and the sampled position in the M87 jet knots. The best-fit slope is shown as a red dashed line and indicated in each panel. Data were taken at the red points in Figure 2. Panels from left to right show significant RM value, close to zero value, and moderate RM value, respectively. We note that the three panels contain thermal noise and the systematic errors mentioned in Section 2.

core is radially symmetric. As for the the core shift contribution, it is only (3 ± 12) mas for M87 core from 86.3 to 100.3 GHz (K. Hada et al. 2011), which is significantly smaller than the synthesized beam size. The asymmetric RM distribution can be caused by the inner jet, including HST-1 (J. A. Biretta et al. 1991), which is $0''.8$ – $0''.9$ offset from the central SMBH (C. C. Cheung et al. 2007; M. Giroletti et al. 2012).

Along the jet from knot D to B, the RM value spans a wide range from $\sim -2 \times 10^4$ rad m $^{-2}$ to $\sim 3 \times 10^4$ rad m $^{-2}$ with a typical error of 0.3×10^4 rad m $^{-2}$. Figure 4 plots the measured EVPAs of the core and the sampled position versus wavelength square of the four subbands. Due to the limited frequency coverage, we adopted a linear fitting to estimate the RM for both the core and the sampled position in the jet knots. The derived RM values are significantly different among the jet knots (Figure 2). The insert panel in Figure 2 illustrates the RM variations on the northern and southern side of the jet axis, as indicated by the red line. The RM curve of both sides is averaged over a width of $1''$ perpendicular to the jet axis. Between knots D and F, the value of RM shows a sequential sign change on both the southern (red) and northern (blue)

sides within a range of $\pm 1.0 \times 10^4$ rad m $^{-2}$. Downstream of knot F, the RM quickly increases on both sides to a peak value of $\sim 2.5 \times 10^4$ rad m $^{-2}$ about half way to knot A and then decreases to a local minimum of $\sim 0.8 \times 10^4$ rad m $^{-2}$ at a distance of $11''.7$ from the core, which is close to the centroid of knot A. Further downstream, taking roughly the same pace on both sides, the RM first rises rapidly to another peak of $\sim 2.3 \times 10^4$ rad m $^{-2}$ immediately post-knot A. A similar, albeit weaker, increasing in the RM in front of knot A was detected at 8–43 GHz by J. C. Algaba et al. (2016), and the location is consistent with the so-called A-shock position (E. S. Perlman et al. 1999; S. S. Avachat et al. 2016). Then the RM drops steeply to a level of $(-0.03 \pm 0.07) \times 10^4$ rad m $^{-2}$ at the centroid of knot B. The RM errors at knots A and B are relatively small due to their high linear polarized intensities.

Toward the more extended structure to knot C, the RM rises again, especially near the northeast side of knot C, where RM values up to $(5.5 \pm 0.6) \times 10^4$ rad m $^{-2}$ are detected. Previous 6 cm observations confirmed an increase in RM at knot C but at a rather lower value of only a few hundred rad m $^{-2}$ (F. N. Owen et al. 1990; J. C. Algaba et al. 2016). In the inner lobes, the RM varies from -2×10^4 to 5×10^4 rad m $^{-2}$

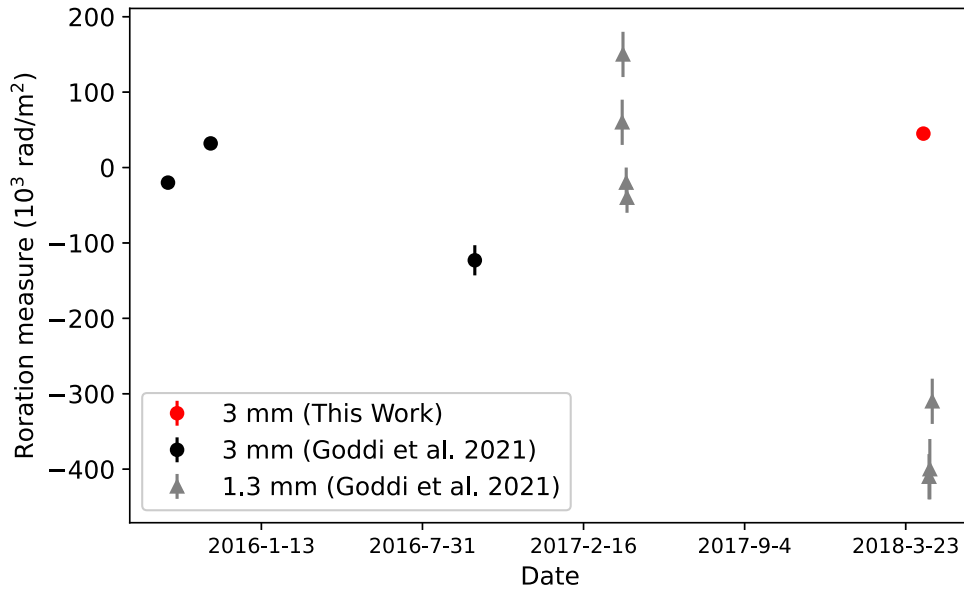


Figure 5. The RM variation in the M87 core from 2015 to 2018 at 3 and 1.3 mm by ALMA observations. Our 3 mm measurement is denoted by the red circle, while the 3 and 1.3 mm measurements by C. Goddi et al. (2021) are denoted by the black circles and gray triangles, respectively.

with a typical error of $0.5 \times 10^4 \text{ rad m}^{-2}$. Previous VLA observations at 6 cm (F. N. Owen et al. 1990) revealed that, on average, the absolute RM values in the inner lobe are higher than those in the jet. We also found RM sign reversals in the inner lobes, which indicate a reversal of the magnetic field direction along the line of sight. This phenomenon has not been detected in previous centimeter observations (F. N. Owen et al. 1990).

4. Discussion

4.1. Faraday RM at the Core

The core exhibits an RM gradient roughly following the jet orientation, in the sense that the southeastern part is 2 times higher than the northwestern part (Figure 2). Due to the limited $1''$ resolution of our observations, it is hard to determine whether such a gradient is due to HST-1 or to the inner milliarcsecond-scale jet (see details in Section 3). However, since HST-1 is optically thin at millimeter wavelengths (C. S. Chang et al. 2010), the RM of the core could be dominated by the milliarcsecond-scale jet or even the inner part. The gradual decrease in electron density along the direction of the jet outward can cause the observed decrease in RM along the northwest direction.

There are two possible origins of the observed Faraday rotation: (1) an internal Faraday screen from an accretion flow (M. Mościbrodzka et al. 2017; Event Horizon Telescope Collaboration et al. 2019; A. Ricarte et al. 2020) and (2) foreground external Faraday screens, including the probable presence of a wind in the vicinity of a jet (J. Park et al. 2019; F. Yuan et al. 2022) or jet sheath (R. T. Zavala & G. B. Taylor 2004; J. C. Algaba et al. 2016; E. Kravchenko et al. 2020). Both the turbulence of the accretion flow and the varying external screen can cause the RM variation. In turn, the variability in RM can help constrain the physical size of the Faraday screen and/or the emitting source (assuming it is variable). For example, C. Goddi et al. (2021) present a model where the RM variability at millimeter wavelengths in M87 can

be explained by a rapidly varying source on the horizon scale and a static Faraday screen.

Figure 5 shows RM measurements by ALMA, including this work and C. Goddi et al. (2019, 2021), from 2016 to 2018 at 1.3 (Band 6) and 3.5 mm (Band 3). Despite the different wavelengths, the ALMA array configuration differences resulted in similar observational resolutions. The RM sign was found to reverse from negative (in 2016) to positive (in 2018), which suggests a change in the core RM sign at least twice over the 2.5 yr period. A remarkable sign reversal occurred between 2018 April 14 and April 21, where within one week the positive RM of $(4.5 \pm 0.4) \times 10^4 \text{ rad m}^{-2}$ at 3 mm changed to negative with a mean RM of $(-4.1 \pm 0.3) \times 10^5 \text{ rad m}^{-2}$ at 1.3 mm. Such a short-term variability implies that the Faraday rotation took place in a very compact region (within 10 Schwarzschild radii, R_{Sch}) in the vicinity of the SMBH. Both an internal Faraday screen introduced by turbulence of accretion flows (M. Mościbrodzka et al. 2017; Event Horizon Telescope Collaboration et al. 2021) and/or a rapid and compact emitting source (C. Goddi et al. 2021) can be used to explain the RM variability with sign reversal on the weekly scale. We caution that the 1.3 and 3.5 mm emissions may not arise from the same location and hence might be subject to a substantially different configuration of the local magnetic field.

In addition to the RM variability, the high ($\sim 10^4 \text{ rad m}^{-2}$) RM detected in our millimeter observations supports a scenario where the Faraday rotation at the core occurs near the SMBH. Previous polarization-sensitive VLBI observations at centimeter wavelengths have probed the RM properties inside the M87 Bondi radius with milliarcsecond resolution. For example, J. Park et al. (2019) found that the absolute RM value at 2–5 GHz increases toward the SMBH, and the value exceeds 1000 rad m^{-2} at a distance of less than $10^4 R_{\text{Sch}}$ from the SMBH. They proposed a wind generated by hot accretion flows as an external Faraday screen and predicted that the RM would be $2 \times 10^4 \text{ rad m}^{-2}$ at a deprojected distance from the SMBH of about $2 \times 10^3 R_{\text{Sch}}$. According to this model, our RM

measurement of $\sim 10^4 \text{ rad m}^{-2}$ could come from a location several thousand R_{Sch} away from the SMBH.

4.2. Faraday RM of the Jet on Arcsecond Scales

As shown in Figure 2, RM sign reversals occur both in the direction parallel to the jet and in the direction perpendicular to the jet from knot D to B. Since the M87 jet has a small viewing angle ($\sim 17^\circ$; C.-C. Wang & H.-Y. Zhou 2009), a change in the pitch angle of the helical magnetic field in the jet can cause RM sign reversals in a direction parallel to the jet. Such RM sign reversals across the jet from knot D to F can be interpreted as a result of the toroidal component of a helical magnetic field in the jet, which has been observed in a number of other active galactic nuclei (AGN) jets, e.g., 3C273 (K. Asada et al. 2002) and 1226+023 (T. Hovatta et al. 2012). Using VLA observations at 4–18 GHz, A. Pasetto et al. (2021) found an RM reversal between knots E and F. We note that this region is also where the transverse RM gradient is most significant in our 3 mm results. We also note that the 3 mm RM signs of the northern and southern parts are opposite to their 4–18 GHz result, which may be due to limited resolution and time variability.

As for knots A and B, polarization fraction, EVPA, and RM change drastically in the upstream of both knots ($10''.7$ and $12''.0$ from the M87 core). This implies that the magnetic field structure is significantly bent upstream of both knots A and B, where in situ magnetic shocks occur (e.g., quad relativistic magnetohydrodynamics shocks; M. Nakamura et al. 2010). As a possible consequence of magnetic field bending, the helical structure of the magnetic field is broken at knot A, and the coil is unwound at knot B (M. Nakamura et al. 2010; E. T. Meyer et al. 2013). This scenario can explain why the 3.5 mm RMs of knots A and B have a similar pattern on the northern and southern sides. Furthermore, RM sign reversals of knot C and the western lobe suggest that the helical structure of magnetic field may slightly remain in these places, supporting the above scenario.

To better understand the jet structure, it would be beneficial to compare our RM measurements at 86–101 GHz with those at other wavelengths. At the lower frequencies of 8–43 GHz, VLA observations revealed RM values of the jet knots at a level of several hundred rad m^{-2} from knot D to knot C (J. C. Algaba et al. 2016). This is 2 orders of magnitude lower than our RM result, although the resolution of our observations ($\sim 2''$) is lower than their VLA observations ($\sim 0''.5$). Assuming the observed RM at different frequencies comes from the same radiation mechanism and that the surrounding environment has a stable magnetic field and a continuous material, such a difference in RM values at different frequencies suggests that the M87 jet is stratified (E. S. Perlman et al. 1999) from millimeter to centimeter wavelengths.

The RM–frequency relationship can be used to estimate the jet geometry. Because of the optical depth effects ($\tau \sim 1$), the thickness of the screen through which the lower-frequency photons pass is smaller. S. G. Jorstad et al. (2007) measured the RM of 15 highly variable AGN jets. Assuming a helical magnetic field, an at least mildly relativistic Faraday screen, and a power-law decreasing gradient in the electron density of the screen, they derived an RM–frequency dependence of $|\text{RM}| \propto \nu^a$. a is related to the profile of a jet electron density (P_{ne}). The jet density profile can be described as a function of distance r from the black hole, $P_{ne} \propto r^{-a}$. For example, $a = 2$

means that the Faraday rotation is occurring in a conically expanding jet, while lower values imply a more highly collimated jet (e.g., S. P. O’Sullivan & D. C. Gabuzda 2009). This relationship can be applied to estimate the geometry of M87 jet. We adopt the range $|\text{RM}| = (0\text{--}250) \text{ rad m}^{-2}$ (with a median of 150 rad m^{-2}) in the frequency range 4–18 GHz (A. Pasetto et al. 2021). For the frequency range 8–43 GHz, we use the range $|\text{RM}| = (0\text{--}500) \text{ rad m}^{-2}$ (with a median of 250 rad m^{-2}) between knot A and D from J. C. Algaba et al. (2016). For the frequency range 86–101 GHz, we use our ALMA result range $\text{RM} = (1\text{--}2.5) \times 10^4 \text{ rad m}^{-2}$. Using an orthogonal distance regression from 4 to 101 GHz, we obtain $\alpha = 2.3 \pm 0.4$ for the kiloparsec-scale jet from knot A to knot D. Our calculated alpha value indicates a trumpet jet shape with an increasingly larger opening angle as the distance from the SMBH increases. This shape corresponds to an overly expanding jet, which likely to happen in a decelerating jet (R. A. Laing & A. H. Bridle 2014).

5. Summary

We have studied the 3 mm ALMA polarization images of the M87 jet. The total intensity and linear polarized intensity are consistent with previous studies (C. Goddi et al. 2021). The average RM value of the core was $(4.5 \pm 0.4) \times 10^4 \text{ rad m}^{-2}$ on 2018 April 14/15. The M87 jet showcases RM values of the order of tens of thousands rad m^{-2} with sign reversals. Time variability and an extreme value of the RM suggest that the Faraday screen at the core is internal, although a rapidly variable-emitting (compact) source could also explain the observed RM. The RM gradient in the jet is consistent with a well-ordered helical magnetic field at the kiloparsec scale (M. Nakamura et al. 2010; S. S. Avachat et al. 2016). A comparison between the 3 mm RM value and measurements at longer wavelengths (J. C. Algaba et al. 2016; A. Pasetto et al. 2021) suggests that the kiloparsec-scale jet between knot A and D has a frequency dependence in RM and that the jet may propagate in a trumpet-like shape.



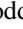








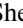
Acknowledgments

We thank Prof. Dr. Eduardo Ros, Dr. Jongho Park, and the anonymous referee for the helpful suggestions. R.L. is supported by the National Science Fund for Distinguished Young Scholars of China (grant No. 12325302), the Key Program of the National Natural Science Foundation of China (grant No. 11933007), the Key Research Program of Frontier Sciences, CAS (grant No. ZDBS-LY-SLH011), the Shanghai Pilot Program for Basic Research, Chinese Academy of Sciences, Shanghai Branch (JCYJ-SHFY-2021-013), and the Max Planck Partner Group of the MPG and the CAS. C.G. acknowledges financial support by the Italian Ministry of University and Research (MUR)– Project CUP F53D23001260001, funded by the European Union – NextGenerationEU and by FAPESP (Fundação de Amparo à Pesquisa do Estado de São Paulo) under grant 2021/01183-8. I.M.-V. acknowledges funding support from Projects PID2022-140888NB-C22 and PID2019-108995GB-C22 (Ministerio de Ciencia, Innovación y Universidades) and Project ASFAE/2022/018 (Generalitat Valenciana). J.Y.K. is supported for this research by the National Research Foundation of Korea (NRF) grant funded by the Korean government (Ministry of Science and ICT; grant No. 2022R1C1C1005255). Z.L. acknowledges support by the National Natural Science Foundation of China

(grant 12225302). R.-Y.L. acknowledges the National Natural Science Foundation of China under grant No. 12393852. This paper makes use of the following ALMA data: ADS/JAO.ALMA#2017.1.00842.V. ALMA is a partnership of ESO (representing its member states), NSF (USA), and NINS (Japan), together with NRC (Canada), MOST and ASIAA (Taiwan), and KASI (Republic of Korea), in cooperation with the Republic of Chile. The Joint ALMA Observatory is operated by ESO, AUI/NRAO, and NAOJ.

Software: APLpy (T. Robitaille & E. Bressert 2012), CASA (CASA Team et al. 2022).

ORCID iDs

Sijia Peng  <https://orcid.org/0000-0001-8492-892X>
 Ru-Sen Lu  <https://orcid.org/0000-0002-7692-7967>
 Ciriaco Goddi  <https://orcid.org/0000-0002-2542-7743>
 Thomas P. Krichbaum  <https://orcid.org/0000-0002-4892-9586>
 Zhiyuan Li  <https://orcid.org/0000-0003-0355-6437>
 Ruo-Yu Liu  <https://orcid.org/0000-0003-1576-0961>
 Jae-Young Kim  <https://orcid.org/0000-0001-8229-7183>
 Masanori Nakamura  <https://orcid.org/0000-0001-6081-2420>
 Feng Yuan  <https://orcid.org/0000-0003-3564-6437>
 Liang Chen  <https://orcid.org/0000-0002-1908-0536>
 Iván Martí-Vidal  <https://orcid.org/0000-0003-3708-9611>
 Zhiqiang Shen  <https://orcid.org/0000-0003-3540-8746>

References

- Algaba, J. C., Asada, K., & Nakamura, M. 2016, *ApJ*, **823**, 86
 Asada, K., Inoue, M., Uchida, Y., et al. 2002, *PASJ*, **54**, L39
 Asada, K., & Nakamura, M. 2012, *ApJL*, **745**, L28
 Avachat, S. S., Perlman, E. S., Adams, S. C., et al. 2016, *ApJ*, **832**, 3
 Bird, S., Harris, W. E., Blakeslee, J. P., & Flynn, C. 2010, *A&A*, **524**, A71
 Biretta, J. A., Stern, C. P., & Harris, D. E. 1991, *AJ*, **101**, 1632
 Blakeslee, J. P., Jordán, A., Mei, S., et al. 2009, *ApJ*, **694**, 556
 Blandford, R., Meier, D., & Readhead, A. 2019, *ARA&A*, **57**, 467
 Blandford, R. D., & Payne, D. G. 1982, *MNRAS*, **199**, 883
 Blandford, R. D., & Znajek, R. L. 1977, *MNRAS*, **179**, 433
 Burn, B. J. 1966, *MNRAS*, **133**, 67
 CASA Team, Bean, B., Bhatnagar, S., et al. 2022, *PASP*, **134**, 114501
 Chang, C. S., Ros, E., Kovalev, Y. Y., & Lister, M. L. 2010, *A&A*, **515**, A38
 Cheung, C. C., Harris, D. E., & Stawarz, Ł. 2007, *ApJL*, **663**, L65
 Clausen-Brown, E., Lyutikov, M., & Kharb, P. 2011, *MNRAS*, **415**, 2081
 Crew, G. B., Goddi, C., Matthews, L. D., et al. 2023, *PASP*, **135**, 025002
 Cui, Y., Hada, K., Kawashima, T., et al. 2023, *Natur*, **621**, 711
 Event Horizon Telescope Collaboration, Akiyama, K., Alberdi, A., et al. 2019, *ApJL*, **875**, L1
 Event Horizon Telescope Collaboration, Akiyama, K., Algaba, J. C., et al. 2021, *ApJL*, **910**, L13
 Garrington, S. T., Leahy, J. P., Conway, R. G., & Laing, R. A. 1988, *Natur*, **331**, 147
 Giroletti, M., Hada, K., Giovannini, G., et al. 2012, *A&A*, **538**, L10
 Goddi, C., Martí-Vidal, I., Messias, H., et al. 2019, *PASP*, **131**, 075003
 Goddi, C., Martí-Vidal, I., Messias, H., et al. 2021, *ApJL*, **910**, L14
 Hada, K., Doi, A., Kino, M., et al. 2011, *Natur*, **477**, 185
 Hada, K., Kino, M., Doi, A., et al. 2016, *ApJ*, **817**, 131
 Hovatta, T., Lister, M. L., Aller, M. F., et al. 2012, *AJ*, **144**, 105
 Hull, C. L. H., Cortes, P. C., Gouellec, V. J. M. L., et al. 2020, *PASP*, **132**, 094501
 Jorstad, S. G., Marscher, A. P., Stevens, J. A., et al. 2007, *AJ*, **134**, 799
 Junor, W., Biretta, J. A., & Livio, M. 1999, *Natur*, **401**, 891
 Kim, J. Y., Krichbaum, T. P., Lu, R. S., et al. 2018, *A&A*, **616**, A188
 Kovalev, Y. Y., Lister, M. L., Homan, D. C., & Kellermann, K. I. 2007, *ApJL*, **668**, L27
 Kraft, R. P., Forman, W. R., Churazov, E. C., et al. 2005, in X-Ray and Radio Connections, ed. L. O. Sjouwerman & K. K. Dyer, **7**, 09
 Kravchenko, E., Giroletti, M., Hada, K., et al. 2020, *A&A*, **637**, L6
 Kuo, C. Y., Asada, K., Rao, R., et al. 2014, *ApJL*, **783**, L33
 Laing, R. A. 1988, *Natur*, **331**, 149
 Läing, R. A., & Bridle, A. H. 2014, *MNRAS*, **437**, 3405
 Lu, R.-S., Asada, K., Krichbaum, T. P., et al. 2023, *Natur*, **616**, 686
 Marshall, H. L., Miller, B. P., Davis, D. S., et al. 2002, *ApJ*, **564**, 683
 Matthews, L. D., Crew, G. B., Doleman, S. S., et al. 2018, *PASP*, **130**, 015002
 Meyer, E. T., Sparks, W. B., Biretta, J. A., et al. 2013, *ApJL*, **774**, L21
 Million, E. T., Werner, N., Simionescu, A., et al. 2010, *MNRAS*, **407**, 2046
 Mościbrodzka, M., Dexter, J., Davelaar, J., & Falcke, H. 2017, *MNRAS*, **468**, 2214
 Nakamura, M., Garofalo, D., & Meier, D. L. 2010, *ApJ*, **721**, 1783
 O’Sullivan, S. P., & Gabuzda, D. C. 2009, *MNRAS*, **393**, 429
 Owen, F. N., Eilek, J. A., & Keel, W. C. 1990, *ApJ*, **362**, 449
 Owen, F. N., Hardee, P. E., & Bignell, R. C. 1980, *ApJL*, **239**, L11
 Park, J., Hada, K., Kino, M., et al. 2019, *ApJ*, **871**, 257
 Pasetto, A., Carrasco-González, C., Gómez, J. L., et al. 2021, *ApJL*, **923**, L5
 Perlman, E. S., Biretta, J. A., Zhou, F., Sparks, W. B., & Macchetto, F. D. 1999, *AJ*, **117**, 2185
 Remijan, A., Biggs, A., Cortes, P., et al., 2019 *LMA Technical Handbook*, *ALMA Doc. 7.3*, v1, Zenodo, doi:10.5281/zenodo.4511522
 Ricarte, A., Prather, B. S., Wong, G. N., et al. 2020, *MNRAS*, **498**, 5468
 Robitaille, T., & Bressert, E., 2012 APLpy: Astronomical Plotting Library in Python, Astrophysics Source Code Library, ascl:1208.017
 Simionescu, A., Tremblay, G., Werner, N., et al. 2018, *MNRAS*, **475**, 3004
 Sparks, W. B., Fraix-Burnet, D., Macchetto, F., & Owen, F. N. 1992, *Natur*, **355**, 804
 Stiavelli, M., Biretta, J., Møller, P., & Zeilinger, W. W. 1992, *Natur*, **355**, 802
 Trippe, S. 2014, *JKAS*, **47**, 15
 Trippe, S., Neri, R., Krips, M., et al. 2010, *A&A*, **515**, A40
 Walker, R. C., Hardee, P. E., Davies, F. B., Ly, C., & Junor, W. 2018, *ApJ*, **855**, 128
 Wang, C.-C., & Zhou, H.-Y. 2009, *MNRAS*, **395**, 301
 Yuan, F., Wang, H., & Yang, H. 2022, *ApJ*, **924**, 124
 Zavala, R. T., & Taylor, G. B. 2004, *ApJ*, **612**, 749